Crystallographic Structure and Crystal Field Parameters in the [An IV (DPA) 3] 2 -series

Matthieu Autillo, Md. Ashraful Islam, Julie Jung, Julien Pilmé, Nicolas Galland, Laetitia Guerin, Philippe Moisy, Claude Berthon, Christelle Tamain, Hélène Bolvin

PCCP

PAPER

Crystallographic Structure and Crystal Field Parameters in the $[An^{IV}(DPA)_3]^{2-}$ series, An= Th, U, Np, Pu.†

Matthieu Autillo[a], Md. Ashraful Islam[b], Julie Jung[c], Julien Pilmé[d], Nicolas Galland[e], Laetitia Guerin[a], Philippe Moisy[a], Claude Berthon[a], Christelle Tamain*[a] and Hélène Bolvin*[b]

The $[An^{IV}(DPA)_3]^{2-}$ series with An = Th, U, Np, Pu has been synthesized and characterized using SC-XRD and vibrational spectroscopy. First principles calculations were performed, the total electron density is analyzed using the Quantum Theory of Atoms in Molecules. Crystal field parameters and strength parameters are deduced following a previous work on the Ln^{III} analog series *e.g.* [Jung J. *et al., Chem. Eur. J.*, 2019, **25**, 15112]. The trends in the parameters along the series are compared to the Ln^{III} complexes. They evidence larger covalent interactions and larger J mixing.

Introduction

The chemical properties of molecules containing actinide ions have been investigated for decades through their involvement in the nuclear fuel cycle as well as in environmental sciences or medical applications [1, 2, 3]. Despite numerous effort, the understanding of this $5f$ elements remains a challenge because of their peculiar electronic structure and radioactive character. Recently, more attention has been devoted to the combination of experimental characterizations and theoretical calculations to elucidate and predict the chemical behavior of actinide compounds. Within the nuclear fuel cycle, plutonium is one of the most involved elements. It displays a very rich and complex chemistry illustrated by the possibility to stabilize five oxidation states in aqueous solution (Pu^{III}, Pu^{IV}, Pu^{V}, Pu^{VI}, Pu^{VII}) [4]. Among them, tetravalent plutonium is the most stable and has been described in multiple systems. While the description of its chemical behavior is challenging when reduced to a single element, the extension to a complete series can strongly improve our understanding. This has been highlighted by recent investigations on Ln^{III} and An^{III} complexes combined to the dipicolinate (DPA) ligand [5, 6, 7, 8]. In the present study, we extend the description of the chemical behavior of actinides with DPA ligands, to ions in the +IV oxidation state for which the increased charge density on the metal is expected to govern the chemistry [4].

We synthesized single crystals of $[An^{IV}(DPA)_3]^{2-}$ complexes of the actinide series (An=Th, U, Np, Pu) following experimental procedure previously described for the Ln^{III} compounds [1]. These solid compounds were subsequently characterized by SC-XRD (Single Crystal X-Ray Diffraction) and vibrational spectroscopy (Raman and IR) to further investigate the metal – ligand interaction. This is the first complete structural characterization of the $[An^{IV}(DPA)_3]^{2-}$ complexes with An=Th, Np, Pu, based on the work of the team of Fedosseev [9, 10].

Ab initio calculations are a useful tool to describe the electronic structure of actinide com-

[a] *CEA, DES, ISEC, DMRC, Univ Montpellier, Marcoule, France*
[b] *Laboratoire de Chimie et Physique Quantiques, CNRS, Université Toulouse III, 118 route de Narbonne, 31062 Toulouse, France.*
[c] *Theoretical division, Los Alamos National Laboratory, Los Alamos, New Mexico 87545, USA.*
[d] *Sorbonne Université, CNRS, Laboratoire de Chimie Théorique CC 137- 4 place Jussieu, 75252 Paris Cédex 05, France.*
[e] *Université de Nantes, CNRS, CEISAM UMR 6230, 44000 Nantes, France.*
* E-mail:christelle.tamain@cea.fr; bolvin@irsamc.ups-tlse.fr
‡ Electronic supplementary information available.

plexes. They help for the understanding of their electronic structure [11, 12], bonding structure [13] and magnetic properties [14, 15, 16, 17] and allow to interpret experimental data. The $[An^{III}(DPA)_3]^{3-}$ series has already been described by SO-CASPT2 (Spin-Orbit Complete Active Space Perturbation Theory at 2nd order) [18] and DFT (Density Functional Theory) [7] methods. The aim of this work is to approach the $[An^{IV}(DPA)_3]^{2-}$ series as we approached the $[Ln^{III}(DPA)_3]^{3-}$ series in our previous work, using crystal field theory [8].

Covalent effects are rather complex to analyze with actinides, and have been the object of many studies [19, 20, 21]. The empty $6d$ metal orbitals play a key role in bonding and charge donation [22, 23]. On the other hand, the $5f$ orbitals are more available to covalent interaction with the ligands due to their larger spatial expansion as compared to the filled $6s6p$ shell. But their shielding by those latter orbitals becomes more and more efficient in the series, with the contraction of the $5f$ orbitals. The Quantum Theory of Atoms-in-Molecules (QTAIM) [24] - known for a long time in the field of non-relativistic quantum calculations - has been used as a complement to the orbital analysis. This approach analyzes the topology of the electron density, the purpose being to answer questions about the chemical bonding and the chemical reactivity. The QTAIM has been successfully applied to actinide complexes described at the DFT level [25, 26]. In this work, the $[An^{IV}(DPA)_3]^{2-}$ complexes are described by the SO-CASPT2 method, and the bonding between the actinide ion and the coordinating atoms is characterized using the QTAIM. For the sake of comparison, the analysis of the SO-CASSCF (Complete Active Space Self-Consistent Field) density in the $[Ln^{III}(DPA)_3]^{3-}$ series is performed as well.

In lanthanide and actinide complexes, the f orbitals are shielded from the ligand interactions by the closed $nsnp$ external orbitals (n = 5 for lanthanides and n = 6 for actinides) and the spectra of the $4f$ and $5f$ ions retain more or less their atomic character. Crystal field theory has been widely used to rationalize the spectroscopic properties of lanthanide complexes, in particular their optical and magnetic properties. Crystal field parameters (CFPs) play a key role in the modelization of pNMR shifts in lanthanide complexes, according to the theory proposed by Bleaney in the 70's [27, 28]. The suitability of the models developed for lanthanide complexes has been questioned early, in particular the capacity of crystal field theory to describe the spectroscopic properties of actinide complexes. Typically, it was recently shown that Bleaney's theory for paramagnetic shifts in lanthanide complexes is not suitable for actinide complexes [18]. In lanthanides, crystal field theory is applied within the limit of very weak field, at either the orbital or many electron level using the Stevens operators. There are few examples of CFPs being determined for An^{IV} complexes. Due to both the strength of the metal - ligand interactions, and the large nuclear charge of the metal center, crystal field interactions are sizable leading to a broad spread of the J manifolds and non-negligible J mixing. CFPs have been determined in octahedral or tetrahedral complexes with halides and oxo ligands [29, 30, 31, 32]. Despite the high symmetry of these compounds, and consecutive reduced number of CFPs, difficulties are encountered in assigning electronic transitions which leads to significant root mean square deviations between the fitted and observed energy levels. There are few examples of CFPs determined from first principles calculations, all of which concern high symmetry complexes: for U^{IV} in octahedral symmetry using LFDFT [33] and for trivalent and tetravalent actinide hexachloride complexes [34].

CFPs are deduced from *ab initio* calculations following either the Ab Initio Ligand Field Theory (AILFT) approach developed by Atanasov [35], or the Irreducible Technique Operators (ITO) approach developed by Ungur and Chibotaru [36]. While the former has already been applied to actinide complexes, the latter has never. The ITO technique is a general mathematical tool, which permits to decompose any square matrix in terms of spherical tensor operators. Using the Wigner-Eckart theorem, the crystal field operator can be expressed in the one-electron manifold, or in many-electron manifolds spanned by the orbital or total angular momenta L or J. The AILFT provides the CFPs at the first level, while the ITO at the second. We showed in our previous work that the CFPs deduced by those two methods are very similar, since the many-electron wave-functions in the complex remain close to the free ion ones, as determined by Clebsch-Gordan coupling coefficients [37]. In the limit of the Russell-Saunders coupling scheme, the two approaches provide the same parameters. In actinide complexes, where the $5f$ orbitals interact more with the ligands orbitals and the J mixing is more important, the use of crystal field theory to the many-electron terms might be questionable. It is one of the aim of this work to answer this question. CFPs are determined using these two techniques, and the ITO technique provide effective parameters including many electron effects and J mixing, the similitude between the CFPs evaluated by the two techniques permit to probe the applicability of the Russel-Saunders coupling scheme to actinide complexes.

In this work, CFPs are deduced from the SO-CASPT2 calculations in the $[An^{IV}(DPA)_3]^{2-}$ series using those two approaches, and the trends are compared to the $[Ln^{III}(DPA)_3]^{3-}$ series and discussed in the light of the QTAIM results. While the

latter theory probes the total density, and characterizes the bonding with all orbitals, CFPs characterize the interaction of the magnetic $5f$ orbitals with the ligands.

The first Section describes experimental and computational details and the second Section discusses the results. Some complementary Tables and Figures are provided in Supplementary Material.

1 Experimental and Computational Section

1.1 Experimental Section

Warning! *^{232}Thorium, ^{238}Uranium, $^{239+240}$Plutonium and ^{237}Neptunium precursors are radioactive and chemically toxic reactants, so precautions with suitable care and protection for handling such substances have been followed. The manipulation of these elements has been carried out at the ATALANTE facility (CEA-Marcoule, France). Because of their highly radioactive nature, the experiments involving Np and Pu were carried out in a regular air atmosphere negative pressure glove box with restrictive protocols, whereas Th and U were manipulated under fume-hood.*

Chemicals – 2,6-pyridinedicarboxylic acid H_2DPA, imidazole, tetraethylammonium chloride, DOWEX resin AG MP1 X8 chloride form, HF 48%, HCl 37% and HNO_3 70% were purchased from Sigma-Aldrich. Solid sodium hydroxide pellets arised from VWR.

Syntheses – Pu^{IV} solution is prepared by dissolving PuO_2 in concentrated nitrofluoric solution (HNO_3 10 M - HF 0.05 M) in glove box. It is then purified by fixation on a DOWEX AG MP1 X8 resin under nitrate form at 7 M HNO_3 and elution with 0.5 M HNO_3. Sodium hydroxide was added to the solution to obtain precipitate and the resultant precipitate was washed with 0.01 M NaOH several times. The stock solution was then prepared by dissolving the washed precipitate in 4 M HCl. The U(IV) chloride solution was prepared by dissolving UO_3 in 4 M HCl followed by electrochemical reduction. The initial solution of neptunium is Np^{V} nitrate solution. Sodium hydroxide was added to the solution to obtain precipitate and the resultant precipitate was washed with water several times. The washed precipitate was then dissolved in 4 M HCl. Np^{V} was reduced electrochemically to allow the preparation of Np^{IV} chloride solution. Oxidation states and concentrations of the actinide solutions were checked by visible spectrophotometry (Agilent Cary 5000 spectrophotometer). A stoichiometric amount of tetraethylammonium chloride was added and the resulting An^{IV} solutions were evaporated under N_2 flow to obtain $(C_8H_{20}N)_2An^{IV}Cl_6$ compounds (An = U, Np and Pu). The starting materials for Th^{IV} and Ce^{IV} was $Th^{IV}(NO_3)_4 \cdot 5\,H_2O$ and $(NH_4)_2Ce(NO_3)_6$ respectively. An aqueous DPA solution was prepared by dissolving 2,6-pyridinedicarboxylic acid (H_2DPA) and imidazole in a 1/2 H_2DPA/Imidazole molar ratio. Starting materials $(C_8H_{20}N)_2An^{IV}Cl_6$ with An = Th, U, Np and Pu, $Th(NO_3)_4 \cdot 5\,H_2O$ and $(NH_4)_2Ce(NO_3)_6$ were dissolved in the DPA solution with a molar ratio An^{IV}/ DPA of 1/5. The resulting solutions were allowed to stand until the deposition of prismatic crystals identified as $[An^{IV}(DPA)_3] \cdot (C_3H_5N_2)_2 \cdot (H_2O)_3$ with An = Th, U, Np and Pu and $[Ce^{IV}(DPA)_3] \cdot (C_3H_5N_2)_2 \cdot (H_2O)_3$.

SC-XRD – Each crystal was mounted on MicroMount patented by MiTeGen, inserted into a goniometer base. To prevent actinide health hazards, a MicroRT capillary was then drawn over the sample and onto the base, where it was sealed by adhesive. The single-crystal XRD intensities were measured on a Bruker D8 Quest diffractometer equipped with a Photon II detector coupled device at 100 K using a 800 series cryostream-cooler (Oxford Cryosystem). The instrument was equipped with a Mo-target IμS Mircofocus source (λ = 0.71073 Å). Data were collected using phi and omega scans, with 1.1° frame widths. Intensities were extracted from the collected frames using the program SAINTPlus [38]. The unit cell parameters were refined from the complete data set, and a multi-scan absorption correction was performed [39]. The structure determination and refinement were realized with shelx-2017 software [40]. The heavy atoms were located by direct methods while the remaining atoms were found from successive Fourier map analyses. All of the non-hydrogen atoms were located and their positions were refined anisotropically. Hydrogen atoms of the DPA molecules were placed in calculated positions refined using idealized geometries (riding model) and assigned fixed isotropic displacement parameters. The hydrogen atoms of the water molecules were placed from Fourier map analyses with O-H distances restrain to 0.8 Å and refined with isotropic displacement parameters.

Raman Spectroscopy – A Jobin−Yvon LabRam Raman 242 spectrometer was used in conjunction with a nuclearized superhead (Optique Peter, Lyon, France) mounted on a support with an objective turret (10x, 20x and 50x). A YAG laser (100 mW, 532 nm) was used with a variable filter to provide low-excitation-beam power levels. The superhead was mounted in a glove box, while the Raman spectrometer and laser were installed outside with a fiber-optic signal transmission line. The microscope objective used for single crystal analyses was 20x.

Table 1: Crystallographic information for compounds **A**, **B**, **C**, **D** and **E**.

	A	**B**	**C**	**D**	**E**
	$C_{27}H_{25}N_7ThO_{15}$ $[Th^{IV}(DPA)_3]\cdot$ $(C_3H_5N_2)_2\cdot(H_2O)_3$	$C_{27}H_{25}N_7UO_{15}$ $[U^{IV}(DPA)_3]\cdot$ $(C_3H_5N_2)_2\cdot(H_2O)_3$	$C_{27}H_{25}N_7NpO_{15}$ $[Np^{IV}(DPA)_3]\cdot$ $(C_3H_5N_2)_2\cdot(H_2O)_3$	$C_{27}H_{25}N_7PuO_{15}$ $[Pu^{IV}(DPA)_3]\cdot$ $(C_3H_5N_2)_2\cdot(H_2O)_3$	$C_{27}H_{25}N_7CeO_{15}$ $[Ce^{IV}(DPA)_3]\cdot$ $(C_3H_5N_2)_2\cdot(H_2O)_3$
Crystal color	colorless	green	brown	red	yellow
Crystal size (μm)	30x70x130	50x40x100	100x50x50	130x180x690	430x270x200
Crystal system	Monoclinic	Monoclinic	Monoclinic	Monoclinic	Monoclinic
Space group	P21/c	P21/c	P21/c	P21/c	P21/c
Z	4	4	4	4	4
FW ($g.mol^{-1}$)	919.58	925.57	924.54	929.54	827.66
a (Å)	9.8122 (6)	9.8225 (8)	9.8352 (4)	9.8486 (4)	9.811 (1)
b Å)	20.445 (1)	20.378 (1)	20.3151 (9)	20.3166 (8)	20.340 (3)
c (Å)	15.9721 (8)	15.902 (1)	15.8431 (7)	15.8306 (6)	15.876 (3)
β(°)	104.283 (2)	104.149 (3)	103.807 (1)	103.965 (1)	104.164 (5)
V ($Å^3$)	3105.2 (3)	3086.4 (4)	3074.0 (2)	3073.9 (2)	3071.8 (8)
Density ($Mg.m^{-3}$)	1.967	1.992	1.998	2.009	1.790
Wavelength (Å)	0.71073	0.71073	0.71073	0.71073	0.71073
μ (mm^{-1})	4.889	5.346	3.468	2.232	1.569
Temperature (K)	100	100	100	100	100
2Θ range (°)	2.142–33.193	2.360–30.534	2.356–30.569	2.355–33.175	2.439–30.574
L.S. parameters, p	475	475	475	475	475
No. of restraints, r	6	6	6	6	2
R/Rw $[I > 2\sigma(I)]$]	0.0251/0.0629	0.0168/0.0426	0.0200/0.0432	0.0184/0.0531	0.0248/0.0737
R/Rw (all data) $[I > 2\sigma(I)]$]	0.0399/0.0755	0.0202/0.0446	0.0277/0.0501	0.0194/0.0544	0.0293/0.0799
Goof	1.096	0.987	1.138	0.958	1.017

Infrared spectroscopy – The solids were analyzed with a dual channel Fourier-Transfom InfraRed (FT-IR) spectrophotometer from Bruker optics, equinox 55, equipped with an ATR module enabling solid samples to be examined directly without further preparation.

1.2 Computational details

MOLCAS calculations – All calculations were carried out on the crystallographic structures. MOLCAS calculations were performed with the version 7.8 suite of programs [41]. ANO-RCC basis sets were used: An QZP, O, N TZP, C DZP and H DZ. Firstly, Spin-Free CASSCF (SF-CASSCF) calculations are performed [42] with an active space composed of the seven $5f$ orbitals of the actinide ion, and associated electrons, i.e. CAS(n,7). For U^{IV} 21 triplets and 28 singlets are considered, for Np^{IV} 35 quartets and 35 doublets, for Pu^{IV} 35 quintets, 60 triplets and 20 singlets. Dynamical correlation is added using the Complete Active Space Perturbation Theory at 2nd order (CASPT2) method [43] with a level shift of 0.3 a.u., either state-specific (SSCASPT2), state by state on the top of the CASSCF wave function or multi-state (MSCASPT2) where a partial decontraction is performed in the active space according to 2nd order. Scalar relativistic effects were taken into account by means of the Douglas-Kroll-Hess transformation [44], and Spin-Orbit (SO) integrals are calculated using the AMFI (Atomic Mean-Field Integrals) approximation [45]. SO coupling is included by a state interaction with the RASSI (Restricted Active Space State Interaction) method [46], the state interaction is calculated either with the CASSCF wave functions giving rise to the SO-CASSCF and SO-SSCASPT2 results or with the MS-CASPT2 wave functions giving rise to the SO-MSCASPT2 results. g factors were calculated according to reference [47] and CFPs were calculated with a local program written in Mathematica as described in references [36, 8].

The Quantum Theory of Atoms-In-Molecules (QTAIM). The molecular space is split into subsystems (basins) which are achieved by applying the theory of dynamical gradient systems to the properties of the electron density. Thus, the basins are associated with each of the atoms in the molecule and are separated by the zero flux surfaces. The topology of the gradient field is characterized by its critical points (CP), where the gradient of the electron density is zero, and by their connectivity. CP can be either maxima (3,-3), minima (3, 3) or saddle points. Among the saddle points, the termed bond critical point (3, -1) (BCP) has a pivotal role because it connects two maxima by only a trajectory of the gradient field (the bond path). In the context of relativistic calculations, QTAIM-based analysis can be used

without any modifications of its current form: this theory is robust enough to resist to modifications of the kinetic energy operator which can differ from a non-relativistic form [48, 49]. Topological descriptors were calculated at the BCP, the density ρ_b, the Laplacian of the electron density $\nabla^2\rho_b$, and the energy densities, kinetic G_b, potential V_b and total $H_b = G_b + V_b$. These latter have been calculated using the Kirzhnits approximation [50]. As has been shown previously [51, 52], the termed relativistic picture change error on the electron density is significant only in the vicinity of heavy atoms and consequently, it does not significantly affect the values of descriptors at the BCP. Topological analyses have been performed using a modified version of the TopMoD09 [53] and TopChem [54, 55] program packages using the total density of the SO-CASPT2 ground state. For the sake of comparison, the SO-CASSCF ground states in the $[Ln^{III}(DPA)_3]^{3-}$ series were considered as calculated in ref [8]. The cube files were obtained with 300*300*300 points.

ORCA calculations – ORCA calculations were performed using the ORCA 4.0.1.2 quantum chemistry package [56]. For the CASSCF calculation, the default CI setting (i.e. CSFCI) was used in combination with the SuperCI and then NR algorithm for the orbital step. Scalar relativistic effects were accounted for using the second-order scalar relativistic Douglas Kroll Hess (DKH2) Hamiltonian formalism [57, 58]. Dynamical correlation was accounted for by using the second order N-electron valence state perturbation theory (NEVPT2) method in its strongly contracted flavor, without frozen core [59, 60, 61]. SO coupling was then accounted for in a mean-field fashion (SOMF) using quasi-degenerate perturbation theory (QDPT) [62], and allowing all CASSCF (SO-free) states from all spin multiplicities to mix through the SOMF operator. To facilitate this task, the CASSCF (SO-free) states were determined using a state-average approach, with all CASSCF states equally weighted. The all electron scalar relativistic TZVPP basis sets [63] were used for the actinide atoms, and the def2-TZVPP basis set [64, 65] for the other atoms (i.e. H, C, N and O). The present def2-TZVPP basis sets are an adapted version of the def2 basis set from the Karlsruhe group (i.e. Ahlrichs basis set) which is provided in the Turbomole basis set library. They retain the original def2 exponents but with contraction coefficients suitable for the DKH scalar relativistic Hamiltonian. Finally, the AUTOAUX feature [66] was used to automatically generate auxiliary basis sets for the resolution of identity approximation (RI-JK) [67], which helps speed up the calculation.

1.3 Crystal field parameters from first principles

Crystal field theory models the splitting of the f orbitals by the field of the ligands surrounding the metal center. This interaction is modeled by tensor operators describing the interaction of f electrons of the actinide ion with the ligands may be described by tensor operators $\hat{O}_k^q$ acting in either the l (one-electron), L (spin-free) or J (SO) manifolds:

$$\hat{V}^{CF}(X) = \sum_{k=2,4,6} \alpha_X^k \sum_{q=-k}^{k} B_q^k \hat{O}_q^k(X) \quad (1)$$

where $X = l, L, J$ according to the considered manifold. The B_q^k are the CFPs, the $\alpha_X^k = \langle X \| \alpha^k \| X \rangle$ are the reduced matrix elements of 2nd, 4th and 6th order respectively. The α_l^k are determined by the number of f electrons N, the α_L^k by N and the orbital angular momentum quantum number L, and the α_J^k by N, L and the total angular momentum quantum number J. These reduced matrix elements are tabulated for the ground state of each lanthanide ion [68] and are similar for the actinide ions with the same number N of unpaired f electrons. The convention of Wybourne is used throughout this work [69, 70]. The CFPs depend on the orientation of the molecule in the $\{X, Y, Z\}$ frame. They are in general imaginary, and rotations around the Z axis affect the phase factor mixing B_q^k and B_{-q}^k. In the present work, Z is chosen as the pseudo rotation axis (see Figure 1), and the choice of the X and Y axes is arbitrary. Hence, only the norm of these parameters is considered in this article [71]

$$\overline{B}_q^k = \sqrt{\left|B_q^k\right|^2 + \left|B_{-q}^k\right|^2} \quad (2)$$

For the sake of comparison, rotational invariants are defined in order to reduce the large number of CFPs to fewer parameters [72, 73].

We considered the strength parameter of kth order

$$S^k = \left[\frac{1}{2k+1} \sum_{q=-k}^{k} \left|B_q^k\right|^2\right]^{1/2} \quad (3)$$

and the strength parameter as defined by Chang [72]

$$S = \left[\frac{1}{3} \sum_{k} \frac{1}{2k+1} \sum_{q=-k}^{k} \left|B_q^k\right|^2\right]^{1/2} \quad (4)$$

These two strength parameters are rotational invariants. In order to quantify the symmetry around the Z axis, the strength parameter of qth index was considered

$$S_q = \left[\sum_{k} \frac{1}{2k+1} \left|B_q^k\right|^2\right]^{1/2} \quad (5)$$

This parameter is not a rotational invariant but it is invariant according to rotations about Z axis. The parameter S allows to evaluate with only one parameter the strength of the ligand field and gives an idea of the overall splitting of the ground J manifold.

CFPs are determined at the orbital level using the *ab initio* ligand field theory (AILFT) developed by Atanasov [35] and implemented in the ORCA code. The correspondence between the model space and the *ab initio* wave function is performed by a recognition of the $5f$ orbitals. Both the *ab initio* and the model Hamiltonians are expanded in the basis of the Slater determinants build from these orbitals. This allows for a one-to-one correspondence with the model space. The model matrix is expressed with the 27 CF matrix elements, the three Slater-Condon parameters for electron-electron repulsion F^2, F^4 and F^6 [74], and the effective one-electron SO coupling parameter ζ. CFPs are also determined from many-electron wave-functions using the ITO method proposed by Ungur and Chibotaru [36]. The decomposition of a square matrix in spin operators equivalent is completely general. One considers the *ab initio* matrix of the Hamiltonian $\mathbf{H}^{AI}$ expanded in the basis of spin matrices $\mathbf{\Omega}_q^{(k)}$ of the ITOs $O_q^{(k)}$ written in the basis of the *ab initio* representative of the $\{|J,M\rangle\}$ kets [75, 76]

$$\mathbf{H}^{AI} = \sum_{k=0}^{2J}\sum_{q=-k}^{k}(-1)^q Q_q^{(k)}\mathbf{\Omega}_{-q}^{(k)} \qquad (6)$$

By comparison with Eq. 1, the expansion coefficients $Q_q^{(k)}$ represent the CFPs B_q^k within the reduced matrix element α_X^k. CFPs deduced from Eq. 6 are effective, in the sense that they provide the energies and wave functions of the ab intio matrix, and consequently include more physical effects than the original crystal field theory, as many-electron and J mixing effects.

CFPs are first deduced at the spin-free level from the $2L+1$ wave-functions and energies arising from the ground ^{2S+1}L term evaluated with SF-CASSCF. Then, with SO coupling, from the $2J+1$ wave-functions and energies arising from the ground J term evaluated with SO-CASSCF, SO-SSCASPT2 and SO-MSCASPT2 methods. Since CFPs are obtained by a decomposition technique, one gets $(2J+1)^2$ coefficients, but this number reduces naturally due to symmetries. The odd order parameters vanish because of time-reversal symmetry and parameters with $k > 6$ vanish in the case of wave functions built from pure f orbitals. The correspondence between the model $|J,M_J\rangle$ kets and the many-electron *ab initio* wave functions is based on the similarity between the *ab initio* $\mathbf{M}_u^J$ $(u = x,y,z)$ and the model $\mathbf{M}_u^{AI}$ matrices of the magnetic moment components operators. In direction u, it might be quantified by the distance between those matrices as

$$\delta m_u = \sqrt{\mathrm{Tr}\left(\mathbf{M}_u^J - \mathbf{M}_u^{AI}\right)^\dagger\left(\mathbf{M}_u^J - \mathbf{M}_u^{AI}\right)} \qquad (7)$$

where Tr denotes the trace and † the conjugate transpose. δm_u vanishes in the limit of the free ion in the LS coupling scheme. An another index, δh, is introduced for quantifying the similarity between the *ab initio* representation matrix and the model matrix up to 6th order:

$$\delta h = \sqrt{\mathrm{Tr}\left(\tilde{\mathbf{H}} - \mathbf{H}^{AI}\right)^\dagger\left(\tilde{\mathbf{H}} - \mathbf{H}^{AI}\right)} \qquad (8)$$

δm_u and δh tend to be zero in the LS coupling scheme limit of the free ion.

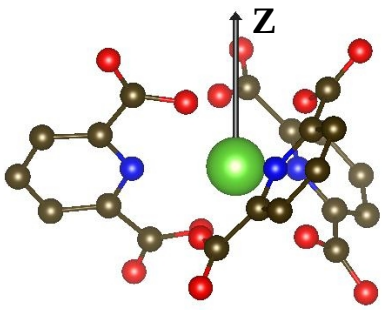

Figure 1: $[An^{IV}(DPA)_3]^{2-}$ complex. Color code: green: An, red: O, blue: N, black: C. Hydrogen atoms have been omitted for clarity.

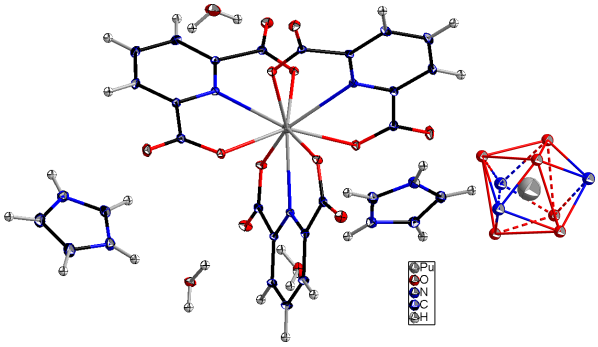

Figure 2: Unit cell content of $[An^{IV}(DPA)_3]\cdot(C_3H_4N_2)_2\cdot(H_2O)_3$ (on the left side) and the corresponding polyhedron (right side). Ellipsoid of 50%.

2 Results and discussion

2.1 X ray structure

The $[An^{IV}(DPA)_3]\cdot(C_3H_5N_2)_2\cdot(H_2O)_3$ compounds with An=Th, U, Np and Pu are isostructural and crystallize in the monoclinic space group $P21/c$

with 4 molecules per unit cell as does the Ce^{IV} analogue (see Table 1). Each actinide cation is coordinated to three tridentate DPA molecules. The ligand is connected through the two carboxylate and the central nitrogen atom. The six oxygen and the three nitrogen atoms form a distorted tricapped trigonal prism with the capped positions occupied by the nitrogen atoms (see Figure 2). The same arrangement has been found in the Ln^{III} series [77, 78, 79, 80, 81, 82, 83, 84, 85, 86, 87, 88, 89, 90, 91], An^{III} series [5, 6, 92] and Ce^{IV} [85, 93] as well as in U^{IV}crystals [9].

The crystal structure of the An^{IV} series and Ce^{IV} derivative evidences closely packed molecules, surrounded by three water molecules as well as two imidazolium cations that ensured the charge compensation (see Figure 3). In addition of the charge compensation, the imidazolium ions are essential to the structure stabilization as they are engaged in multiple intermolecular interactions (see Figure 3). Indeed, $\pi - \pi$ interactions can be identified between two neighboring imidazolium cations, and between imidazolium cations and DPA ligands with a distance of 3.1 and 3.24 – 3.34 Å, respectively. The counter-ions are also involved in hydrogen bonds with the free water molecules (in the range 2.69(1) – 2.71(1) Å) and the oxo oxygen (between 2.68(1) and 2.71(1) Å). Hydrogen bonds connecting the free water molecules and the oxo group (in a range 2.75(1) – 2.96(1) Å) and several free water molecules (2.78(1) Å) can also be observed and complete this large intermolecular interaction network. Among this network, one of the DPA molecule of the $[An^{IV}(DPA)_3]^{2-}$ unit is not involved in $\pi - \pi$ interactions. This non-interacting DPA molecule presents similar geometrical parameters as the others and suggests that there is no influence of this intermolecular interaction network on the first coordination sphere bond distances.

From Th^{IV} to Pu^{IV}, the An^{IV}–O and An^{IV}–N distances decrease from 2.427 to 2.354 Å and from 2.598 to 2.500 Å, respectively (see Table 2). These distances are comparable to the U^{IV} structure of Grigoriev (2.376(1) and 2.540(1) Å) [9]. Those distances follow the ionic radii contraction (see Figure 4), and the trends are linear, which indicates that there is no brutal change in their complexation behavior across the An^{IV} series. $[Ln^{III}(DPA)_3]^{3-}$ structures have been described across the whole $4f$ series with $[Co(NH_3)_6]^{3-}$ as counter ion. The absence of significant modification induced by intermolecular interactions on the first coordination sphere distances justify the comparison of the two f element series. Structure characteristics for those two series are given in Table 2. M–O and M–N bond distances are represented against the ionic radii in Figure 4 as a first qualitative analysis for trends in the series. We considered ionic radii as determined by Shannon with CN = 9 [94] for Ln^{III}, Th^{IV} and U^{IV} and by Choppin for $Np^{IV}$and Pu^{IV} [97]. The Ln^{III}–O and Ln^{III}–N distances also decrease linearly with the ionic radii. It is interesting to note that the Ln^{III}-O and An^{IV}-O distances are similar for the same ionic radius whereas the An^{IV}–N distances are significantly longer ($\approx$ 0.1 Å) than the Ln^{III}–N distances. The simple analysis of the metal–oxygen bond distances in these compounds does not reflect the harder Lewis acid character expected for An^{IV} cations. However, we can notice that Ce^{IV}–O and Ce^{IV}–N bond distances and geometrical parameters also fit the linear An^{IV} series.

In order to get some insight on the interaction strength between the metal and the ligand, we analyzed $C_1 - O_1$ bond distances across both series, where O_1 is the coordinating oxygen atom (see Figure 5). In the An^{IV} structures, the $C_1 - O_1$ distances are all close to 1.285(2) Å and are in accordance with the previously described $[U^{IV}(DPA)_3] \cdot (H_2O)_3 \cdot (C_6H_{12}(NH_3)_2)$ compound [9]. This is longer by 0.02 Å than for Ln^{III} complexes (1.268(5) Å). The lengthening of the $C_1 - O_1$ bond brings out a larger donation due to a stronger charge transfer towards the An^{IV} cation. The $O_1 - O_1^{'}$ shortens between the free ligand and the coordinated one: 4.8(1) Å for H_2DPA and 4.26(2) Å for the An^{IV} structures. Similarly, this distance decreases from 4.456 to 4.303 Å along the Ln^{III} series. As a consequence, the bite angles NC_2C_1 and $O_1NO_1^{'}$ close with complexation, and a loss of planarity of the ligand is highlighted by a torsion angle $O_1C_1C_1^{'}O_1^{'}$ up to 11°. Since the bite angle is more closed in the An^{IV} derivatives, for the same $M - O_1$ distance, the $M - N$ distance is longer in a An^{IV} than in a Ln^{III}. Geometrical parameters in the Ce^{IV} complex are very similar to those of the An^{IV} ones, which shows that the effective charge of the metal plays a determinant role in the deformation of the ligand.

2.2 Raman and FT-IR spectra

To investigate the metal-ligand interaction in DPA complexes, the Raman and FT-IR solid state spectra of the $[An^{IV}(DPA)_3] \cdot (C_3H_5N_2)_2 \cdot (H_2O)_3$ and $[Ce^{IV}(DPA)_3] \cdot (C_3H_5N_2)_2 \cdot (H_2O)_3$ complexes as well as the solid H_2DPA and imidazole compounds were collected at room temperature (see Figures 6 and S1).

On the Raman spectra of solid H_2DPA compound, the $C_1 = O_2$ stretching vibration appears as a strong band at 1641 cm^{-1} while the $C_1 - O_1$ stretching vibration is much weaker and located at 1151 cm^{-1} as previously reported [98]. The multiplication of weak bands on An^{IV} complexes spectra makes a confident assignment of the $C_1 - O_1$ stretching frequency difficult and is therefore not

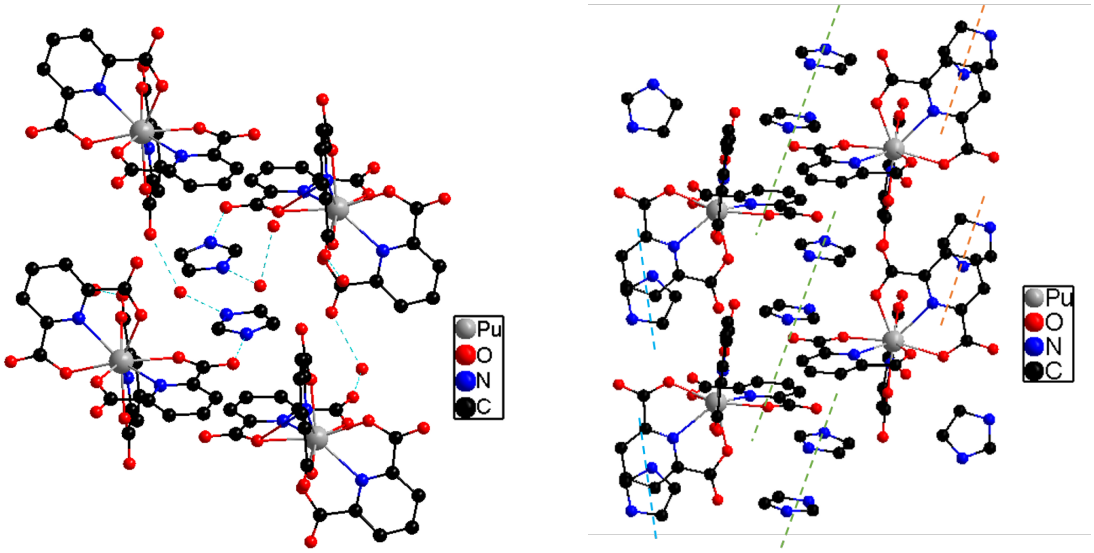

Figure 3: $[Pu^{IV}(DPA)_3] \cdot (C_3H_5N_2)_2 \cdot (H_2O)_3$ structure. Intermolecular interactions are represented by dashed lines : hydrogen bonds on the left side and $\pi - \pi$ interaction on the right side. For the last one, water molecules were omitted for clarity.

Table 2: Distances (in Å) and angles (in °) of $[An/Ce^{IV}(DPA)_3] \cdot (C_3H_5N_2)_2 \cdot (H_2O)_3$ structures compared to structures from the literature of H_2DPA and $[Ln^{III}(DPA)_3]^{3-}$. The atoms are labeled after Figure 5.

	ionic radii [a]	distances					angles		torsion angle
		$<M-O_1>$	$<M-N>$	$<C_1=O_2>$	$<C_1-O_1>$	$<O_1\cdots O_1'>$	NC_2C_1	O_1NO_1'	$O_1C_1C_1'O_1'$
Th^{IV} **(A)**	1.09	2.427	2.598	1.233	1.283	4.296	114.2	111.2	8.31
U^{IV} **(B)**	1.05	2.380	2.543	1.232	1.287	4.252	113.9	110.6	8.06
Np^{IV} **(C)**	1.03	2.368	2.513	1.233	1.285	4.258	114.0	110.5	7.81
Pu^{IV} **(D)**	1.01	2.354	2.500	1.233	1.285	4.240	113.9	110.3	7.10
Ce^{IV} **(E)**	1.02±0.01 [b]	2.357	2.516	1.231	1.286	4.231	113.8	110.1	7.73
U^{IV} [c]	1.05	2.376	2.540	1.229	1.287	4.248	113.9	110.5	4.25
H_2DPA [d]	-	-	-	1.239	1.285	4.841	116.6	121.0	2.6
H_2DPA [e]	-	-	-	1.247	1.275	4.719	116.6	122.5	1.0
La^{III} [f,g]	1.216	2.540	2.644	1.241	1.260	4.456	115.5	114.6	5.05
Ce^{III} [f,g]	1.196	2.521	2.634	1.242	1.265	4.426	115.0	114.0	5.41
Pr^{III} [f,g]	1.179	2.503	2.598	1.244	1.266	4.432	115.2	114.0	5.57
Nd^{III} [g]	1.163	2.473	2.562	1.236	1.267	4.402	115.0	113.7	8.21
Sm^{III} [g]	1.132	2.457	2.541	1.238	1.263	4.391	114.6	113.5	5.59
Eu^{III} [f]	1.12	2.440	2.526	1.274	1.274	4.377	115.8	113.0	7.32
Gd^{III} [f]	1.107	2.435	2.516	1.261	1.261	4.367	114.5	113.1	7.93
Tb^{III} [f,g]	1.095	2.424	2.499	1.269	1.269	4.366	114.5	112.9	6.43
Ho^{III} [f]	1.072	2.396	2.477	1.275	1.275	4.345	114.7	112.2	7.19
Er^{III} [e]	1.062	2.395	2.463	1.253	1.274	4.337	114.2	112.4	5.84
Tm^{III} [f,g]	1.052	2.376	2.448	1.235	1.265	4.314	114.2	112.1	9.28
Yb^{III} [f]	1.042	2.372	2.439	1.246	1.269	4.313	113.9	112.0	10.87
Lu^{III} [f,g]	1.032	2.361	2.425	1.239	1.275	4.303	113.9	111.8	9.88

a: from ref. [94]. *b* : The Ce^{IV} ionic radii with CN = 9 is not known. Nevertheless for CN = 6, 8 or 10, $R_{Pu^{IV}} < R_{Ce^{IV}} < R_{Np^{IV}}$. The ionic radii given in this table are considered as the average of the Np^{IV} and Pu^{IV} radii with a CN of 9. *c*: from ref. [85]. *d*: from ref. [95]. *e*: from ref. [96]. *f*: from ref. [77]. *g*: from ref. [78].

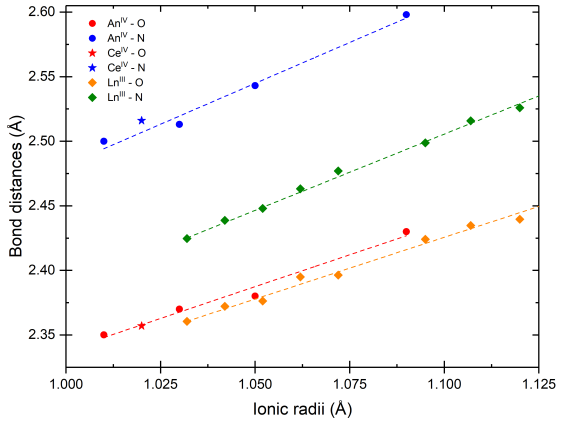

Figure 4: Evolution of first coordination sphere distances (An^{IV}–O and An^{IV}–N) in $[An^{IV}/Ce^{IV}(DPA)_3] \cdot (C_3H_5N_2)_2 \cdot (H_2O)_3$ and $[Ln^{III}(DPA)_3]^{3-}$ compounds according to their respective ionic radii for CN=9.

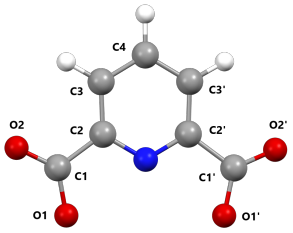

Figure 5: DPA ligand with the numbering of the atoms.

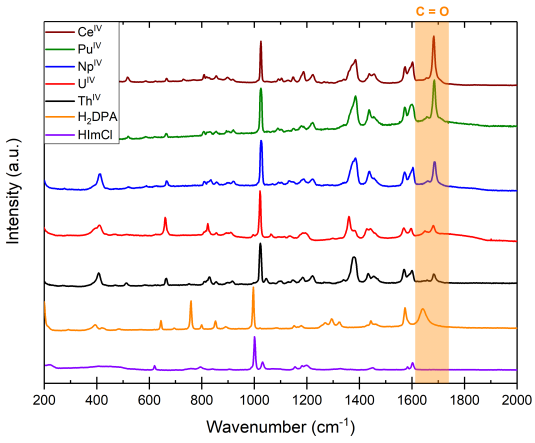

Figure 6: Raman spectra of $[An/Ce^{IV}(DPA)_3] \cdot (C_3H_5N_2)_2 \cdot (H_2O)_3$ for An=Th, U, Np and Pu, H_2DPA and imidazolium chloride.

discussed. Because of the electronic delocalization along the carboxylic function, the $C_1 = O_2$ stretching frequency can be used to analyze the $C_1 - O_1 \cdots An^{IV}$ interaction. The Raman spectra of the $[An^{IV}(DPA)_3] \cdot (C_3H_5N_2)_2 \cdot (H_2O)_3$ single crystals reveal unshifted $C_1 = O_2$ stretching vibrations across the actinide series at 1684(1) cm^{-1}. An^{IV} complexation induces a stabilization of the $C_1 = O_2$ bond resulting in a blue shift of its corresponding stretching vibration of 41 cm^{-1} compared to the free ligand. This aspect is in agreement with the non-evolution of the $C_1 = O_2$ bond distances from Th^{IV} to Pu^{IV} in the XRD crystal structures, and confirms that the strength of the hydrogen bond that involves this oxygen atom is also unchanged. The spectrum corresponding to the isostructural Ce^{IV} complex is almost identical with a $C_1 = O_2$ stretching vibration at 1683 cm^{-1}. This similarity between An^{IV} and Ce^{IV} complexes associated to unchanged bond distances supports a complexation behavior predominantly affected by the actinide effective charge. The non evolution of distances and frequencies of the C=O is quite unusual for this type of carboxylate compounds.

2.3 Energy of the states

First principles calculations were performed for the $[An^{IV}(DPA)_3]^{2-}$ series on the crystallographic structure with SF-CASSCF, SO-CASSCF, SO-NEVPT2 and SO-CASPT2 methods. At the SO free level, the states arising from a LS free ion term split due to the interaction with the ligands, but the splitting is smaller than the energy difference between two LS terms, and the states of the complex may be labeled after the free ion LS term. At SO level, the free ion J terms are rather close in energy, the J mixing is important, and the different J manifolds overlap. The identification of the states after their free ion J term might not be possible for the excited states, but at the least, the manifold arising from the ground J term is well separated from others, its splitting will be discussed in the following, and it will be used for the calculation of the CFPs in Section 2.5. SO free energies are given in Table 3, the SO energies, in Table 4, and the standard deviation between methods, in Table S2.

The ground LS term spreads over about 2800 cm^{-1} for U^{IV}, about 3500 cm^{-1} for Np^{IV}, and about 4000 cm^{-1} for Pu^{IV}. It is much larger than for the Ln^{III} complexes because the $5f$ orbitals interact more with the ligands orbitals and because the charge of the metal is larger. For comparison, the splitting is in the 500 cm^{-1} range for the $[Ln^{III}(DPA)_3]^{3-}$ series. The SF-CASSCF energies obtained with the two programs (ORCA and MOLCAS) are identical for the spin-free states arising from the ground LS term, and very similar for the

Table 3: Energies (cm^{-1}) of the SO free states in the $[An^{IV}(DPA)_3]^{2-}$ series. Different LS manifolds are separated by a vertical line.

method	E_1	E_2	E_3	E_4	E_5	E_6	E_7	E_8	E_9	E_{10}	E_{11}	E_{12}	E_{13}	E_{14}	E_{15}	E_{16}	E_{17}	E_{18}
										U^{IV}								
SF-CASSCF [a]	0	317	412	628	992	994	1457	1566	2534	2644	2796	5219	5320	5348	5781	5800	5809	6020
SF-CASSCF [b]	0	321	417	643	1006	1008	1466	1575	2544	2655	2799	5195	5240	5295	5685	5712	5779	6000
SF-SSCASPT2 [a]	0	107	233	346	425	588	1230	1257	2187	2315	2669	3828	3857	4152	4208	4459	4485	4567
SF-MSCASPT2[a]	0	139	236	587	823	930	1591	1656	2463	2660	2976	4145	4181	4316	4460	4499	4734	4880
SF-NEVPT2 [b]	0	210	349	751	1100	1138	1757	1882	2934	3001	3153	3900	4012	4482	4557	5046	5430	5448
										Np^{IV}								
SF-CASSCF [a]	0	243	262	1096	1133	1439	1772	2056	2108	2554	2768	2826	3377	11674	11682	11810	11866	11985
SF-CASSCF [b]	0	240	258	1093	1130	1443	1775	2058	2109	2554	2772	2833	3383	11580	11589	11704	11760	11869
SF-SSCASPT2 [a]	0	253	357	1084	1213	1233	1660	2087	2092	2797	2804	3001	3593	9092	9215	9243	9841	10012
SF-MSCASPT2 [a]	0	321	616	1092	1377	1498	1835	2174	2351	2930	2996	3246	3769	9264	9416	9445	9952	10084
SF-NEVPT2 [b]	0	308	352	1404	1459	1809	2201	2593	2668	3154	3424	3502	4000	8003	8190	8251	9141	9158
										Pu^{IV}								
SF-CASSCF [a]	0	888	939	1096	1589	1640	1762	2253	2473	2505	3186	3204	3460	12192	12816	12889	12938	13096
SF-CASSCF [b]	0	889	944	1106	1598	1649	1776	2261	2491	2526	3205	3225	3475	12044	12671	12747	12790	12952
SF-SSCASPT2 [a]	0	685	774	888	1233	1316	1522	2250	2500	2582	3365	3425	4013	10023	10469	10691	10691	11050
SF-MSCASPT2 [a]	0	679	761	889	1238	1434	1622	2283	2530	2706	3412	3509	4084	10067	10493	10752	10752	11168
SF-NEVPT2 [b]	0	1221	1301	1586	2156	2225	2407	3043	3343	3392	4201	4242	4605	9147	9315	9885	9934	10223

a: calculated with MOLCAS. b: calculated with ORCA.

Table 4: Energies (in cm^{-1}) of the first excited states including SO coupling in $[An^{IV}(DPA)_3]^{2-}$ series. Different J manifolds are separated by a vertical line.

method	E_1	E_2	E_3	E_4	E_5	E_6	E_7	E_8	E_9	E_{10}	E_{11}	E_{12}	E_{13}	E_{14}	E_{15}	E_{16}
										U^{IV}						
SO-CASSCF [a]	0	47	197	211	354	443	938	1042	1496	5328	5345	6095	6108	6184	6260	6487
SO-CASSCF [b]	0	41	201	218	346	442	945	1049	1499	5335	5352	6115	6125	6221	6309	6518
SO-SSCASPT2 [a]	0	100	194	230	236	316	843	966	1413	4789	4805	5235	5267	5380	6301	6371
SO-MSCASPT2 [a]	0	221	229	300	338	421	975	1105	1606	4294	4401	5136	5171	5289	6289	6510
SO-NEVPT2 [b]	0	85	238	258	426	543	1091	1205	1731	4545	4578	4816	4892	4905	6371	6414
										Np^{IV}						
SO-CASSCF [a]	0	0	138	138	517	517	999	999	1245	1245	6009	6009	6045	6045	6200	6200
SO-CASSCF [b]	0	0	138	138	517	517	991	991	1247	1247	6079	6079	6117	6117	6269	6269
SO-SSCASPT2 [a]	0	0	89	89	474	474	938	938	1225	1225	6173	6173	6222	6222	6403	6403
SO-MSCASPT2 [a]	0	0	44	44	464	464	894	894	1196	1196	6084	6084	6188	6188	6289	6289
SO-NEVPT2 [b]	0	0	161	161	606	606	1154	1154	1456	1456	6389	6389	6426	6426	6600	6600
										Pu^{IV}						
SO-CASSCF [a]	0	96	460	467	557	700	1039	1078	1388	4853	4935	4988	5247	5264	5337	5339
SO-CASSCF [b]	0	95	460	465	556	682	1021	1059	1344	5103	5179	5229	5455	5464	5552	5560
SO-SSCASPT2 [a]	0	109	512	528	628	704	1109	1162	1545	4977	5037	5091	5438	5464	5495	5515
SO-MSCASPT2 [a]	0	149	524	583	612	726	1151	1236	1521	4991	5088	5134	5414	5497	5528	5537
SO-NEVPT2 [b]	0	119	526	537	647	855	1262	1304	1653	5457	5556	5621	5914	5929	6043	6060

a: calculated with MOLCAS. b: calculated with ORCA.

excited LS terms. The CASPT2 and NEVPT2 energies are different, which is expected since the two methods are based on different formalisms. The energies of the ground LS term are generally larger with NEVPT2 than with CASPT2 hence leading to a larger overall splitting of the ground term with NEVPT2. SSCASPT2 and MSCASPT2 do not provide the same energies: with SSCASPT2, the perturbation is calculated individually for each CASSCF state while with MSCASPT2, an effective coupling between the CASSCF states is estimated, hence leading to different wave-functions and different energies. With all methods, the perturbation increases the spread of the ground LS term while the energy of the second LS manifold is lowered, due to a larger compactness of the electron density, and consequently a larger dynamical correlation. The largest deviation between NEVPT2 and CASPT2 is reached for the U^{IV} complex, especially for SSCASPT2 with a deviation of 700 cm^{-1}. The deviation between the different methods is about 100 cm^{-1} for the ground LS manifold, and can reach 1000 cm^{-1} for the 2nd LS manifold.

At SO level, the SO-CASSCF energies obtained with the two codes are identical; this confirms that the calculation of the SO coupling is equivalent in the two codes, as was already checked for the p block [99]. At the PT2 level, the inclusion of dynamical correlation does not impact strongly the overall splitting of the ground J term, but it impacts the energy of the different states arising from this term. With SO coupling, the overall splitting of the ground J term is 1500 cm^{-1}, to be compared to 300 cm^{-1} in the analog Ln^{III} series. This splitting depends only slightly on the method: with SO-NEVPT2, it is always larger than with SO-CASSCF, and more generally, all energies of the ground J manifold are larger. Conversely, there is no systematic trend for CASPT2: it may decrease or increase the energy of the second J manifold, depending on the method.

Contrarily to the energy difference between two spin-free LS terms which arises from two-electron interactions and consequently are affected by dynamical correlation, the energy difference between two J manifolds arising from the same LS term is due to SO coupling, which is mostly a one-electron interaction. It is impacted by 2nd order interactions through J mixing, which are more important for actinides than for lanthanides. The standard deviation in the SO energies calculated by the different perturbative methods is rather small, even for a large number of roots. The J mixing can be evaluated from the composition of the SO wave functions in terms of the LS states. The weight on the ground LS manifold of ground J SO functions is 88 % for the three complexes at SO-CASSCF level, and 86 % at SO-CASPT2 level. In all cases, the J mixing occurs mostly with a state of spin $S_{max} - 1$ (^1G for U^{IV}, ^2H for Np^{IV} and ^3H for Pu^{IV}); this should be compared to 98 % in the $[Ln^{III}(DPA)_3]^{3-}$ series.

Magnetic properties depend on both the wave function and the energy of the low lying states, and may differ sensibly with the method of calculation. This is specially the case for U^{IV} and Pu^{IV} which have an even number of electrons. In this case, without spatial symmetry, the SO states are not degenerated and non magnetic. Magnetic properties arise from the coupling with excited states through the Zeeman interaction. Hence, the energy gap between these states is determinant for the magnetic properties [100]. In actinide complexes, the gap is much larger than in lanthanides, about 100 cm^{-1}, as in the present case. For the Np^{IV} complex, the ground state is a Kramers doublet, which is characterized by the g factors. One gets 2.82, 2.46, 1.92 with CASSCF, 2.73, 2.61, 1.93, with SS-CASPT2, and 3.43, 1.28, 0.42 with MSCASPT2: the MS-CASPT2 values are different since this method affects the composition of the wave-functions.

The energies calculated in the $[An^{IV}(DPA)_3]^{2-}$ series with SO-CASSCF, SO-CASPT2 and SO-NEVPT2 methods show that the states arising from the ground free ion J manifold are well separated from other manifolds. The overall splitting of this manifold is larger with the PT2 methods. The distribution of the SO states in the ground J manifold differ by up to 100 cm^{-1}, which impacts the calculated magnetic properties and, perforce, the CFPs as described in Section 2.5.

2.4 QTAIM topological analysis

The ground state total density was analyzed by the mean of QTAIM approach, together with the SO-CASSCF and SO-CASPT2 wave functions in the $[Ln^{III}(DPA)_3]^{3-}$ and $[An^{IV}(DPA)_3]^{2-}$ series. The computed descriptors at the BCP of the bonds between the central metal and the coordinating oxygen and nitrogen atoms are given in Table S3. It is acknowledged in the QTAIM framework that both a ρ_b density larger than 0.20 a.u. and a negative Laplacian $\nabla^2\rho_b$ are typical of shared-shell interactions between atoms, that is (mainly) covalent bonds. Conversely, we found here typical values of closed-shell interactions. ρ_b is always lower than 0.10 a.u. and $\nabla^2\rho_b$ is markedly positive, i.e. there is a depletion of the charge density at the BCP of each M–O and M–N interaction. Hence, all those values show a ionic or donor-acceptor type interaction, in accordance with previous QTAIM analysis on actinide complexes [25, 19, 101, 26]. The ionic nature of the M–O and M–N bonds is also supported by the computed QTAIM charges, which reflect highly polarized bonds. Indeed, the Ln^{III} and An^{IV} ions bear very positive charges, around

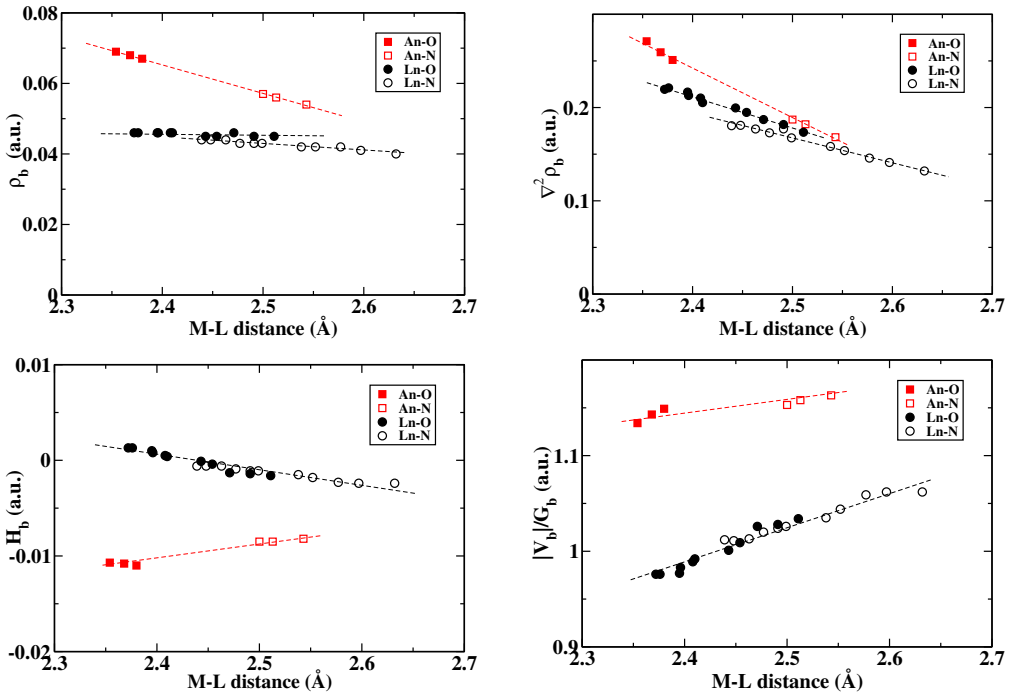

Figure 7: QTAIM descriptors ρ_b, $\nabla^2\rho_b$, H_b and $|V_b|/G_b$ at the BCPs for the M-O and M-N bonds in the $[Ln^{III}(DPA)_3]^{3-}$ and $[An^{IV}(DPA)_3]^{2-}$ series. The dashed lines indicate the trends.

2.5 and 3.2 electrons, respectively, while the coordinating oxygen and nitrogen atoms bear marked negative charges, around -1.4 and -1.3 electrons, respectively.

The ρ_b values for the bonds involving An^{IV} ions are at least 20% stronger than for the bonds involving Ln^{III} ions, which confirms that the bonding with the DPA ligands is stronger for the former. A $|V_b|/G_b$ ratio at the BCP larger than 1, as well as a negative value of H_b, indicate some covalent contribution [102]. Indeed, the potential energy density V_b is the leading term vs. the positive definite kinetic energy density G_b, hence electrons are stabilized at the BCP. $|V_b|/G_b$ is larger than 1 for An^{IV}–N and An^{IV}–O bonds, but it is smaller for for Ln^{III}–N bonds and eventually lower than 1 for some Ln^{III}–O bonds. Although weak (the total energy H_b is overall very close to zero), the magnitude of covalency is more pronounced for interactions mediated by the An^{IV} ions than by the Ln^{III} ions. The relativistic effects due to the SO coupling interaction on the ground state density have also been assessed. As an example, Table S3 reports the descriptors values obtained for the spin-free wave functions of $[Tm^{III}(DPA)_3]^{3-}$ and $[U^{IV}(DPA)_3]^{2-}$, for the latter within single-state and average-state schemes. Trifling differences with respect to previous values can be noticed, showing no significant effects of the SO interaction on the bonding patterns.

The descriptors are represented against the bond distance in Figure 7. The trends for the four descriptors with the bond length are roughly linear, with distinct trends for Ln^{III} and An^{IV}. ρ_b at the BCP of Ln^{III}–O bonds seems rather constant while it slowly decreases with the bond length for Ln^{III}–N ones, meaning that Ln^{III}–N bonds slightly strengthen along the series. The effect of the distance is more pronounced for the bonds with An^{IV}: ρ_b depends only on the distance between the An^{IV} cation and the coordinating atom, whether an oxygen or nitrogen atom, and increases when the distance shortens. Regarding the $|V_b|/G_b$ descriptor in the Ln^{III} series, it decreases as the bond length shrinks, eventually becoming lower than 1 for some Ln^{III}–O interactions, indicating a pure ionic character in late lanthanides. In the An^{IV} series, $|V_b|/G_b$ is rather constant, independently on the nature of the coordinating atom. It shows a small decrease towards the end of the series, which is in favor of a small decrease of the covalent effects. Hence, according to the QTAIM analysis, with the shrinking of the coordination sphere, An^{IV} and Ln^{III} ions tend to form stronger interactions, and more ionic in the case of Ln^{III}.

QTAIM and LoProp charges are compared in Table S3. Note that the partition of the total density into atomic contributions is not unequivocal. QTAIM atomic charges are calculated as the integration of the density over atomic basins, which are defined from zero-flux surfaces partitioning the 3D total density [24]. LoProp charges are obtained after a localization procedure, organized into a series of orthogonalizations of the original basis set [103]. The metallic charges determined by the two methods are very similar, around 2.5 for Ln^{III} and 3.2 for An^{IV}, but the charges on the coordinating

oxygen and nitrogen atoms are much larger with QTAIM than with LoProp. It shows that the partition of the density between the metal and the three ligands is the same with QTAIM and LoProp, but the partition inside each ligand strongly differ. This mostly concerns the nitrogen atoms. With LoProp, the nitrogen charge is much smaller than the oxygen one, leading to a closer picture to the chemical intuition (oxygen is more electronegative and the charge located on the COO^- moiety). While the charges of the coordinating atoms are constant in the series, the metal charge, as depicted in Figure S2, shows small variations, with opposite trends with the two methods. The QTAIM metal charge is a little bit erratic in the lanthanide series, but the global trend is a decrease along the series. Actually, the QTAIM metal charge follow the trend of the metal basin volume, which follows the contraction of the coordination sphere along the two series. According to LoProp charges, the ligand to metal electron donation decreases in the series, while QTAIM predicts the opposite behavior. This charge analysis was completed by a Mulliken population analysis which gives the distribution of the electrons par type of orbital (see Table S4). From U^{IV} to Pu^{IV}, the An charge increases from 3.17 to 3.21 denoting a more ionic bond. The donation to the f orbitals decreases (0.55-0.46), partially compensated by the increase of the donation to the d orbitals (1.10-1.15). This is due to the more rapid contraction of the $5f$ than the $6d$ orbitals and the 5f orbitals are more filled.

To conclude, the QTAIM and other charge analysis show that the metal-ligand interaction is stronger in the An^{IV} series than in the Ln^{III}one: the interaction is strongly ionic, with slightly larger covalent effects for actinides. The interaction increases slightly in the two series, with a small decrease of the covalent effects for Ln^{III} complexes.

2.5 Crystal Field Parameters

The CFPs have been deduced from the *ab initio* calculations using both the AILFT and the ITO methods. The largest strength parameters are represented in Figures 8 and all CFPs are given in Table S6 of the SI. The Slater-Condon and SO parameters are given in Figures 9 and Table S7. As in the $[Ln^{III}(DPA)_3]^{3-}$ series, the variation are rather smooth, such that one can consider the CFPs to be transferable. In agreement with Equation 1, the α^k are determined by the central metal ion and the B_q^k by the ligands. The CFPs are strongly dominated by the 4th and 6th orders parameters. The 2nd order strength parameter S^2 is around 300 cm^{-1}, against 150 cm^{-1} in the Ln^{III} series, while the 4th and 6th orders S^4 and S^6 are around 1200 cm^{-1}, against 300 cm^{-1} in the Ln^{III} series. The CFPs determined

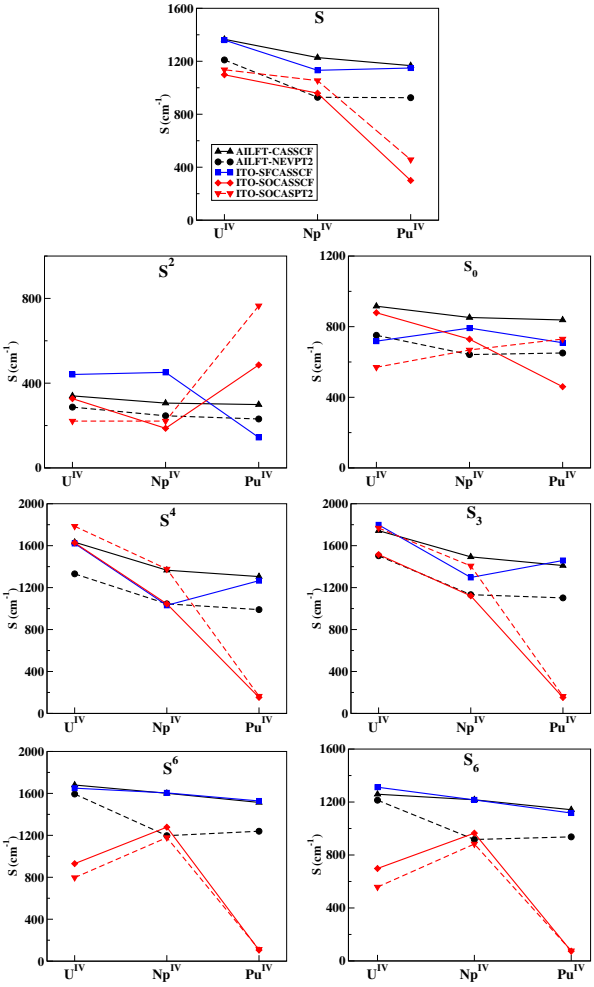

Figure 8: Strength parameters of the $[An^{IV}(DPA)_3]^{2-}$ series calculated with different methods.

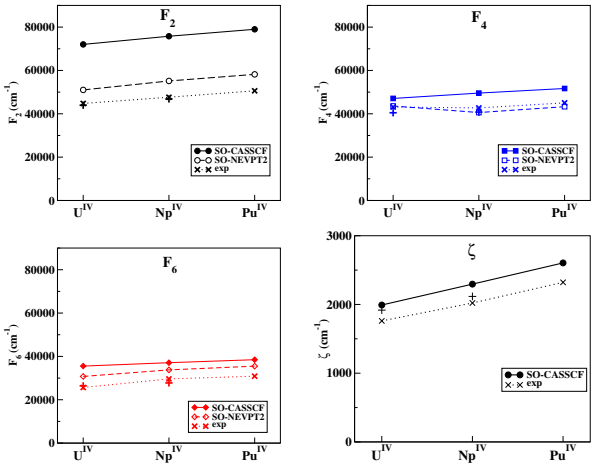

Figure 9: Slater-Condon parameters and SO coupling parameter ζ in cm^{-1} calculated with AILFT in the $[An^{IV}(DPA)_3]^{2-}$ series. .

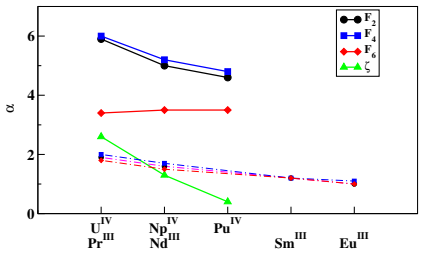

Figure 10: Nephelauxetic reduction factors (%) calculated with AILFT in the $[Ln^{III}(DPA)_3]^{3-}$ (dashed, [8]) and $[An^{IV}(DPA)_3]^{2-}$ (plain) series. Free-ion data are taken from ref. [34].

by Krupta and Carnall, for different halide and oxo An^{IV} compounds, by fitting optical spectra, are of the same order of magnitude as the parameters in the present study [29, 104, 30]. The Condon-Slater parameters increase in the series in accordance with the contraction of $5f$ orbitals and to the increase of the number of electrons. F^4 and F^6 are similar to the experimental ones while F^2 is larger, as it was the case for the $[An^{III}Cl_6]^{3-}$ [34]. As discussed in ref. [34], it might be due to the incomplete description of the dynamical correlation, and to the different definition of the parameters, since the fitting of experimental data include more terms, as for example three body terms. The SO coupling parameter ζ is slightly overestimated with respect to experiment, but the trend is the same. It increases in the series following the increase of the nuclear charge and follows the trends described in ref. [34]. The nephelauxetic reduction factors $((1 - p/p^{FI}) * 100$ where p and p^{FI} represent the property in the complex and in the free ion respectively) for inter-electronic repulsion integrals and the SO coupling parameter have been deduced, and compared to the Ln^{III} analog series, using the free ion values of ref. [34] in Figure 10. This reduction arise from covalent effects, both due the delocalization on the ligands and to a the better shielding the nucleus [105]. At the CASSCF level, the reduction is about 5%, which is slightly smaller than in the $[An^{III}Cl_6]^{3-}$ series, where it is about 6%, but much larger than in the Ln^{III} analog series where for the beginning of the series, it is only worth 2%. It is much smaller than in $3d$ transition metal complexes [106]. The reduction factor deduced from ζ is smaller and decreases much faster.

While S^2, S^4 and S^6 are rotation invariants, the S_q strength parameters are not. Z axis is chosen to be orthogonal to the plane formed by the three nitrogen atoms. As in $[Ln^{III}(DPA)_3]^{3-}$ series, the dominant CFPs are S_0, S_3 and S_6, in accordance with the trigonal symmetry. B_0^2 is positive while B_0^4 and B_0^6 are negative. The total strength parameter S is reduced in the ITO method from U^{IV} to Pu^{IV} with a sharp decrease for Pu^{IV} in the SO calculation. CFPs extracted from ITO method are not as uniform, since these are effective parameters that have been generated from the many-electron wave functions. The CFPs may be deduced from the ground L manifold using SF-CASSCF energies and wave-functions: at this level, the ITO CFPs contain many-electron effects, which are included in the Slater-Condon parameter in the AILFT method. At the SO-CASSCF level, they are deduced from the ground J manifold and then, the ITO CFPs additionally contain the J mixing with excited LS terms. The SF-CASSCF/ITO CFPs are very close to the CASSCF/AILFT ones; this shows that the building of the many-electron function from the $5f$ orbitals is close to that of the free ion as in lanthanide complexes [37]. But the SO-CASSCF/ITO differ slightly from the SF-CASSCF/ITO ones due to the larger J mixing in the actinide complexes, which also tends to reduce the total strength parameter. This effect is more pronounced for the Pu^{IV} derivative, most likely because Pu^{IV} holds more f electrons, and hence, a richer electronic structure. PT2 does not impact strongly.

The ITO CFPs are based on the similitude of the $2J+1$ *ab initio* states with those of the angular momentum J, as quantified in Table S5. The method relies on the decomposition of the matrix representation of the Hamiltonian in terms of ITOs according to Equation 6. The odd orders of this expansion disappear due to Kramers symmetry and the expansion sums up to 8th order in the case of $J = 4$ or $9/2$. In the frame of crystal field theory, with wave functions built with pure f orbitals, the terms of orders larger than 6 vanish due to the $3j$ symbol selection rules. The larger δh, the more important terms of 8th order are. In Table S5, the values of δh are larger than in the Ln^{III} analog series, but are still reasonably small, which proves the reminiscence of the free ion electronic structure. The largest δh are found for the Pu^{IV} derivative, when SO coupling is included, in accordance with the CFPs for the Pu^{IV} derivative being more different between AILFT and ITO. While δh is worth at most 40 cm^{-1} in the Ln^{III} series, it is worth up to 100 cm^{-1} in the An^{IV} series. It shows that the 8th order terms are not completely negligible in actinide complexes: the effect of the 8th order on the matrix elements and eigenvalues is of several 10 of cm^{-1}. This might have a quantitative effect but the fundamentals of crystal field theory keeps qualitatively correct for those actinide complexes.

In our previous study, it was shown that the decrease of the strength parameter in the $[Ln^{III}(DPA)_3]^{3-}$ series arises from covalent effects in their general meaning, namely any orbital effect including bonding, charge donation and polarization. Even in the ionic crystal $PrCl_3$, covalent effects were shown to be important. Covalent effects are even more complex to analyze with actinides, and have been the object of many studies

[19, 20, 21]. The empty $6d$ metal orbitals play a key role for bonding and charge donation [22, 23], $5f$ orbitals are more available to covalent interaction with the ligands due to their larger spatial expansion as compared to the filled $6s6p$ shell. But the shielding becomes more and more efficient in the series, with the contraction of the $5f$ orbitals. The impact of covalent effects has been discussed throughout this work and can be summarizes as follow: i) The nephelauxetic reduction factors are larger than in the Ln^{III} series and decrease from U^{IV} to Pu^{IV}. ii) The QTAIM descriptor $|V_b|/G_b$ slightly decreases in the series. iii) Figure S3 compares the variation of the strength parameter with respect to the ionic radius $\Delta S/\Delta R$: the decrease in the $[An^{IV}(DPA)_3]^{2-}$ series is much faster than in the $[Ln^{III}(DPA)_3]^{3-}$ series. iv) The charge analysis denotes a decrease of the ligand to metal charge transfer. v) We have observed in previous studies on lanthanide species [37, 8] that the 2nd order S^2 is dominant and corresponds to a pure electrostatic picture, but tend to decrease in favor of the S^4 and S^6, once the covalent effects are incorporated. In the present case, the 4th and 6th orders are very important. All together, this indicates that covalent effects are larger in the actinide series and tend to decrease from U^{IV} to Pu^{IV}.

Conclusion

The $[An^{IV}(DPA)_3]^{2-}$ series has been synthesized, and characterized by SC-XRD. It is shown than the metal-oxygen bond is similar to the $[Ln^{III}(DPA)_3]^{3-}$ analog with the same ionic radius, while the metal-nitrogen distance is elongated. Intermolecular interactions do not impact the coordination sphere. *Ab initio* calculations were performed on the X-rays geometries. The QTAIM analysis confirms the ionic nature of the bonding and shows that the interactions tend to be stronger and more ionic along the series. It is shown that the SO coupling does not affect the bonding and that the interaction is stronger than in the analog lanthanide series. SO-NEVPT2 and SO-CASPT2 energetic spectra are similar, and the weight on the LS ground terms is evaluated to be 88 %, much lower than in the Ln^{III} analog series. The AILFT provide CFPs deduced at orbital level, whose meaning is close from the original crystal field theory. They show a smooth behavior, similarly to those deduced at spin-free many electron level. As in the Ln^{III} series, the magnitude of the CFPs also tend to decrease, but the decrease is steeper. The nephelauxetic reduction factors related to Slater-Condon and SO parameters decrease.

The ITO decomposition has been applied for the first time to calculate CFPs in actinide complexes. The expansion coefficients provide effective CFPs whose physical meaning incorporate many electron effects and J mixing. The smallness of the CFPs of order larger than 6 and the likeness of the ab initio magnetic moment matrices with those of a spin operator consolidate the use of this technique. In spin-free calculations the CFPs seem to be transferable but the addition of SO coupling makes it difficult to conclude. CFPs deduced from SO coupling calculations are more irregular, which is most likely a consequence of significant J mixing. Notably for the Pu^{IV} complex that is most affected by the J mixing, although quantitatively similar as for the two other complexes. The CFPs are of the same order of magnitude than those fitted on experimental optical spectra [29, 104, 30]. They are larger than their Ln^{III} analogs, and the CFPs of 4th and 6th orders are important. This makes the spectra of actinide complexes more difficult to be anticipated, since the B_0^2 is by far not dominant. B_0^2 is related to the prolate or oblate shape of the coordination sphere. When B_0^2 is dominant, one can predict with simple rules the anisotropy of the magnetic properties, like the single molecule magnets properties or the pseudo-contact term for paramagnetic shifts through Bleaney's theory. Furthermore, due to the J mixing, the spectra can not be anticipated since it scrambles the energetic spectra and consequently the properties. It means that the set of CFPs deduced from many-electron manifolds depend strongly on the J manifold. As already concluded for the Ln^{III} series, the many electron CFPs, since they effectively account for all interactions are suitable to reproduce the magnetic properties which arise only from the ground J manifold. Furthermore, the CFPs reproduce the energy ordering and composition of those states avoiding the calculation of the interaction with excited states. On the other hand, the orbital CFPs are more appropriate for the modeling of optical spectra, since they are unequivocal. It is then possible to calculate the whole spectrum using the Slater-Condon and SO parameters.

Acknowledgments

This work was supported by the ANR under convention N°ANR-17-CE06-0010. This work was sponsored by the US DOE through the LANL. LANL is operated by Triad National Security, LLC, for the NNSA of US DOE (Contract No. 89233218NCA000001). J.J. thanks LANL for funding through the Director's Postdoctoral fellowship. This work was supported by the National Science Foundation under grant CHE-1361799 to VLP. P. M. thanks A. Fedosseev and M. Grigoriev for the fruitful discussions concerning the synthesis of An^{IV} single crystals.

Associated Content CCDC 1968862 (A), 1968863 (B), 1968864 (C), 1968865 (D) and 1968863 (E)

contain the supplementary crystallographic data for this paper. This data can be obtained free of charge from the Cambridge Crystallographic Data Centre via www.ccdc.cam.ac.uk/data_request/cif. Supporting information for this article including crystallographic data and IR spectra is available.

References

[1] Choppin, G. Actinide speciation in the environment. *J. Radioanal. Nucl. Chem.* **2007**, *273*, 695–703.

[2] Ansoborlo, E.; Prat, O. Actinide speciation in relation to biological processes. *Biochimie* **2006**, *88*, 1605–1618.

[3] Nesmerak, K. Lanthanide/Actinide in Health and Disease. In *Encyclopedia of Metalloproteins*; Kretsinger, R.; Uversky, V.; Permyakov, E., Eds.; Springer: New York, NY,.

[4] Clark, D.; Hecker, S.; Jarvinen, G.; Neu, M. Plutonium. In *Encyclopedia of Metalloproteins*; Morss, L.; Edelstein, N.; Fuger, J., Eds.; Springer: Netherlands,.

[5] Cary, S. K.; Vasiliu, M.; Baumbach, R. E.; Stritzinger, J. T.; Green, T. D.; Diefenbach, K.; Cross, J. N.; Knappenberger, K. L.; Liu, G.; Silver, M. A.; ; DePrince, A. E.; Polinski, M. J.; Cleve, S. M. V.; House, J. H.; Kikugawa, N.; ; Gallagher, A.; Arico, A. A.; Dixon, D. A.; Albrecht-Schmitt, T. E. Emergence of californium as the second transitional element in the actinide series. *Nat. Commun.* **2015**, *6*, 1–8.

[6] Silver, M. A.; Cary, S. K.; Johnson, J. A.; Baumbach, R. E.; Arico, A. A.; Luckey, M.; Urban, M.; Wang, J. C.; Polinski, M. J.; Chemey, A.; Liu, G.; Chen, K. W.; Van Cleve, S. M.; Marsh, M. L.; Eaton, T. M.; van de Burgt, L. J.; Gray, A. L.; Hobart, D. E.; Hanson, K.; Maron, L.; Gendron, F.; Autschbach, J.; Speldrich, M.; Køgerler, P.; Yang, P.; Braley, J.; Albrecht-Schmitt, T. E. *Science* **2016**, *353*, 888.

[7] Kelley, M. P.; Su, J.; Urban, M.; Luckey, M.; Batista, E. R.; Yang, P.; Shafer, J. C. On the origin of covalent bonding in heavy actinides. *J. Am. Chem. Soc.* **2017**, *139*, 9901–9908.

[8] Jung, J.; Islam, M. A.; Pecoraro, V. L.; Mallah, T.; Berthon, C.; Bolvin, H. Derivation of lanthanide series crystal field parameters from first principles. *Chem. Eur. J.* **2019**, *25*, 15112–15122.

[9] Grigoriev, M. S.; Fedosseev, A. M. private communication,.

[10] Yusov, A. B.; Fedoseev, A. M. Complexation of tetravalent actinides (Th, U, Np, Pu) with 2,6-pyridinedicarboxylic acid in aqueous solutions.. *Radiochemistry* **2013**, *55*, 360–365.

[11] Gendron, F.; Autschbach, J. Electronic Structure of the Actinide Elements. In *Encyclopedia of Inorganic and Bioinorganic Chemistry*; R. A. Scott (Ed.): , 2018.

[12] Dolg, M., Ed.; *Computational methods in lanthanide and actinide chemistry;* Wiley: , 2015.

[13] Atkinson, B. E.; Hu, H.-S.; Kaltsoyannis, N. Post Hartree-Fock calculations of pnictogen-uranium bonding in EUF3 (E = N-Bi). *Chem. Commun.* **2018**, *54*, 11100–11103.

[14] Páez Hernàndez, D.; Bolvin, H. Magnetic properties of a fourfold degenerate state: Np^{4+} ion diluted in Cs_2ZrCl_6 crystal. *J. Electron. Spectrosc. Relat. Phenom.* **2014**, *194*, 74.

[15] Coutinho, J. T.; Antunes, M. A.; Pereira, L. C. J.; Bolvin, H.; Marçaloa, J.; Mazzanti, M.; Almeida, M. Single-ion magnet behavior in [U(TpMe2)2I]. *Dalton Trans* **2012**, *41*, 13568.

[16] Autillo, M.; Guerin, L.; Bolvin, H.; Moisy, P.; Berthon, C. Magnetic susceptibility of actinide(III) cations: Experimental and theoretical study. *Phys. Chem. Chem. Phys.* **2016**, *18*, 6515.

[17] Dey, S.; Rajaraman, G. In silico design of pseudo D5h actinide based molecular magnets: role of covalency in magnetic anisotropy. *J. Chem. Sci.* **2019**, 124.

[18] Autillo, M.; Guerin, L.; Dumas, T.; Grigoriev, M. S.; Fedoseev, A. M.; Cammeli, S.; Solari, P. L.; Guilbaud, P.; Moisy, P.; Bolvin, H.; Berthon, C. Insight of the metal-ligand interaction in f elements complexes by paramagnetic NMR spectroscopy. *Chem. Eur. J.* **2019**, *25*, 4435.

[19] Kaltsoyannis, N. Does covalency increase or decrease across the actinide series? Implications for minor actinide partitioning. *Inorg. Chem.* **2013**, *52*, 3407–3413.

[20] Neidig, M. L.; Clark, D. L.; Martin, R. L. Covalency in f-element complexes. *Coord. Chem. Rev.* **2013**, *257*, 394 – 406.

[21] Lu, E.; Sajjad, S.; Berryman, V.; Wooles, A. J.; Kaltsoyannis, N.; Liddle, S. T. Emergence of the structure-directing role of f-orbital overlap-driven covalency. *Nat. Commun.* **2019**, *10*, 634.

[22] Bolvin, H.; Wahlgren, U.; Gropen, O.; C., M. Ab initio study of the two iso-electronic molecules NpO_4^- and UO_4^{2-}. *J. Phys. Chem. A* **2001**, *3*, 10570.

[23] Bursten, B. E.; Palmer, E. J.; Sonnenberg, J. L. Recent Advances in Actinide Science. In ; Eds. May, I. and Bryan, N. D. and Alvares, R.: The Royal Society of Chemistry, London, 2006.

[24] Bader, R. F. W. *Atoms in Molecules: A quantum theory;* Oxford University Press: New York, 1994.

[25] Vallet, V.; Wahlgren, U.; Grenthe, I. Probing the nature of chemical bonding in uranyl(VI) complexes with quantum chemical methods. *J. Phys. Chem. A* **2012**, *116*, 12373–12380.

[26] Wellington, J. P.; Kerridge, A.; Kaltsoyannis, N. Should environmental effects be included when performing QTAIM calculations on actinide systems? A comparison of QTAIM metrics for Cs2UO2Cl4, U(Se2PPh2)4 and Np(Se2PPh2)4 in gas phase, COSMO and PEECM. *Polyhedron* **2016**, *116*, 57–63.

[27] Bleaney, B.; Dobson, M.; Levine, B. A.; Martin, R. B.; Williams, R. J. P.; Xavier, A. V. Origin of lanthanide nuclear magnetic resonance shifts and their uses. *J. Chem. Soc. Chem. Comm.* **1972**, *13*, 791–793.

[28] Bleaney, B. Nuclear magnetic resonance shifts in solution due to lanthanide ions. *J. Magn. Reson.* **1972**, *8*, 91.

[29] Krupa, J. Spectroscopic properties of tetravalent actinide ions in solids. *Inorg. Chim. Acta* **1987**, *139*, 223–241.

[30] Carnall, W. T.; Liu, G. K.; Williams, C. W.; Reid, M. F. Analysis of the crystal field spectra of the actinide tetrafluorides. I. UF4, NpF4, and PuF4. *J. Chem. Phys.* **1991**, *95*, 7194–7203.

[31] Liu, G. K.; Carnall, W. T.; Jursich, G.; Williams, C. W. Analysis of the crystal field spectra of the actinide tetrafluorides. II. AmF4, CmF4, Cm4+:CeF4, and Bk4+:CeF4. *J. Chem. Phys.* **1994**, *101*, 8277–8289.

[32] Faucher, M. D.; Moune, O. K.; Garcia, D.; Tanner, P. Evidence for strong interaction between the $5f^2$ and $5f^17p^1$ configurations of U^{4+} in the octahedral sites of Cs_2UBr_6 and Cs_2ZrBr_6. *Phys. Rev. B* **1996**, *53*, 9501–9504.

[33] Ramanantoanina, H.; Kuri, G.; Daul, C.; Bertsch, J. Core electron excitations in U^{4+}: modelling of the $nd^{10}5f^2 \rightarrow nd^9\ 5f^3$ transitions with n = 3, 4 and 5 by ligand field tools and density functional theory. *Phys. Chem. Chem. Phys.* **2016**, *18*, 19020–19031.

[34] Jung, J.; Atanasov, M.; Neese, F. Ab Initio ligand-field theory analysis and covalency trends in actinide and lanthanide free ions and octahedral complexes. *Inorg. Chem.* **2017**, *56*, 8802–8816.

[35] Atanasov, M.; Zadrozny, J. M.; Long, J. R.; Neese, F. A theoretical analysis of chemical bonding, vibronic coupling, and magnetic anisotropy in linear iron(ii) complexes with single-molecule magnet behavior. *Chem. Sci.* **2013**, *4*, 139–156.

[36] Ungur, L.; Chibotaru, L. F. Ab Initio crystal field for lanthanides. *Chem. Eur. J.* **2017**, *23*, 3708–3718.

[37] Alessandri, R.; Zulfikri, H.; Autschbach, J.; Bolvin, H. Crystal field in rare-earth complexes: from electrostatics to bonding. *Chem. Eur. J.* **2018**, *24*, 5538–5550.

[38] SAINTPlus; version 6.22; Bruker Analytical X-ray Systems: Madison, WI, 2001.

[39] SADABS, version 2.03; Bruker Analytical X-ray Systems: Madison, WI, 2001.

[40] SHELX-97.

[41] Aquilante, F.; De Vico, L.; Ferré, N.; Ghigo, G.; Malmqvist, P.-A.; Neogrády, P.; Pedersen, T. B.; Pitonak, M.; Reiher, M.; Roos, B.; Serrano-Andrés, M.; Urban, M.; Veryazov, V.; Lindh, R. MOLCAS 7: The next generation. *J. Comput. Chem.* **2010**, *31*, 224.

[42] Roos, B. O.; Taylor, P. R.; Siegbahn, P. E. M. A complete active space SCF method (CASSCF) using a density matrix formulated super-CI approach. *Chem. Phys.* **1980**, *48*, 157.

[43] Andersson, K.; Malmqvist, P.-A.; Roos, B. O.; Sadlej, A. J.; Wolinski, K. Second-order perturbation theory with a CASSCF reference function. *J. Phys. Chem.* **1990**, *94*, 5483.

[44] Hess, B. A. Relativistic electronic-structure calculations employing a two-component no-pair formalism with external-field projection operators. *Phys. Rev. A* **1986**, *33*, 3742.

[45] Hess, B. A.; Marian, C. M.; Wahlgren, U.; Gropen, O. A mean-field spin-orbit method applicable to correlated wavefunctions. *Chem. Phys. Lett.* **1996**, *251*, 365.

[46] Malmqvist, P.-A.; Roos, B. O.; Schimmelpfennig, B. The restricted active space (RAS) state interaction approach with spin-orbit coupling. *Chem. Phys. Lett.* **2002**, *357*, 230.

[47] Bolvin, H. An alternative approach to the g-matrix: theory and applications. *ChemPhysChem* **2006**, *7*, 1575.

[48] Anderson, J. S. M.; Ayers, P. W. Quantum Theory of Atoms in Molecules: Results for the SR-ZORA Hamiltonian. *J. Phys. Chem. A* **2011**, *115*, 13001–13006.

[49] Anderson, J. S. M.; Ayers, P. W. The general setting for the zero-flux condition: The lagrangian and zero-flux conditions that give the Heisenberg equation of motion. *J. Comput. Chem.* **2018**, *39*, 1051–1058.

[50] Kirzhnits, D. A. Quantum corrections to the Thomas-Fermi equation. *Sov. Phys.* **1957**, *JETP 5*, 64.

[51] Eickerling, G.; Mastalerz, R.; Herz, V.; Scherer, W.; Himmel, H.-J.; Reiher, M. Relativistic effects on the topology of the electron density. **2007**, *3*, 2182–2197.

[52] Bučinský, L.; Kucková, L.; Malček, M.; Kožíšek, J.; Biskupič, S.; Jayatilaka, D.; Büchel, G. E.; Arion, V. B. Picture change error in quasirelativistic electron/spin density, Laplacian and bond critical points. *Chem. Phys.* **2014**, *438*, 37–47.

[53] Noury, S.; Krokidis, X.; Fuster, F.; Silvi, B. Computational tools for the electron localization function topological analysis. *Comput. Chem.* **1999**, *23*, 597–604.

[54] Kozlowski, D.; Pilmé, J. New insights in quantum chemical topology studies using numerical grid-based analyses. *J. Comput. Chem.* **2011**, *32*, 3207–3217.

[55] http://www.lct.jussieu.fr/pagesperso/pilme/topchempage.html (accessed on April 4, 2020).

[56] Neese, F. Software update: the ORCA program system, version 4.0. *Wiley Interdisciplinary Reviews: Computational Molecular Science 8*, e1327.

[57] Reiher, M. Douglas-Kroll-Hess theory: a relativistic electrons-only theory for chemistry. *Theor. Chem. Acc.* **2006**, *116*, 241–252.

[58] Nakajima, T.; Hirao, K. The Douglas-Kroll-Hess approach. *Chem. Rev.* **2012**, *112*, 385–402.

[59] Angeli, C.; Cimiraglia, R.; Evangelisti, S.; Leininger, T.; Malrieu, J.-P. Introduction of n-electron valence states for multireference perturbation theory. *J. Chem. Phys.* **2001**, *114*, 10252–10264.

[60] Angeli, C.; Cimiraglia, R.; Malrieu, J.-P. N-electron valence state perturbation theory: a fast implementation of the strongly contracted variant. *Chem. Phys. Lett.* **2001**, *350*, 297–305.

[61] Angeli, C.; Cimiraglia, R.; Malrieu, J.-P. n-electron valence state perturbation theory: A spinless formulation and an efficient implementation of the strongly contracted and of the partially contracted variants. *J. Chem. Phys.* **2002**, *117*, 9138–9153.

[62] Neese, F. Efficient and accurate approximations to the molecular spin-orbit coupling operator and their use in molecular g-tensor calculations. *J. Chem. Phys.* **2005**, *122*, 034107.

[63] Pantazis, D. A.; Neese, F. All-electron scalar relativistic basis sets for the actinides. *J. Chem. Theory Comput.* **2011**, *7*, 677–684.

[64] Weigend, F.; Furche, F.; Ahlrichs, R. Gaussian basis sets of quadruple zeta valence quality for atoms H–Kr. *J. Chem. Phys.* **2003**, *119*, 12753–12762.

[65] Weigend, F.; Ahlrichs, R. Balanced basis sets of split valence triple zeta valence and quadruple zeta valence quality for H to Rn: Design and assessment of accuracy. *Phys. Chem. Chem. Phys.* **2005**, *7*, 3297–3305.

[66] Stoychev, G. L.; Auer, A. A.; Neese, F. Automatic generation of auxiliary basis sets. *J. Chem. Theory Comput.* **2017**, *13*, 554–562.

[67] Neese, F. An improvement of the resolution of the identity approximation for the formation of the Coulomb matrix. *J. Chem. Theory Comput.* **2003**, *24*, 1740–1747.

[68] Abragam, A.; Bleaney, B. *Electronic paramagnetic resonance of transition ions;* Clarendon Press: Oxford, 1970.

[69] Wybourne, B. G. *Spectroscopic Properties of Rare Earths;* Wiley-Interscience: New-York, 1965.

[70] Görller-Walrand, C.; Binnemans, K. Chapter 155 Rationalization of crystal-field parametrization. In *Handbook on the Physics and Chemistry of Rare Earths*, Vol. 23; Elsevier: , 1996.

[71] Rudowicz, C.; Qin, J. Noether's theorem and conserved quantities for the crystal- and ligand-field Hamiltonians invariant under continuous rotational symmetry. *Phys. Rev. B* **2003**, *67*, 174420.

[72] Chang, N. C.; Gruber, J. B.; Leavitt, R. P.; Morrison, C. A. Optical spectra, energy levels, and crystal-field analysis of tripositive rare earth ions in Y2O3. I. Kramers ions in C2 sites. *J. Chem. Phys.* **1982**, *76*, 3877–3889.

[73] Yeung, Y. Y. Invariants and moments. In *Crystal field handbook*; Newman, D. J.; Ng, B. K. C., Eds.; Cambridge University Press: , 2000.

[74] Griffith, J. S. *The theory of transition metal ions;* Cambridge University Press: Cambridge, 1961.

[75] Zare, R. N. *Angular momentum;* Wiley: New-York, 1988.

[76] Van den Heuvel, W.; Soncini, A. NMR chemical shift as analytical derivative of the Helmholtz free energy. *J. Chem. Phys.* **2013**, *138*, 054113.

[77] Harrowfield, J.; Ling, I.; Skelton, B.; Sobolev, A.; White., A. *Aust. J. Chem.* **2017**, *70*, 485.

[78] Brayshaw, P.; Hall, A.; Harrowfield, W. H. J.; Pearce, D.; Shand, T.; Skelton, B.; Whitaker, C.; White, A. *Eur. J. Inorg. Chem.* **2005**, 1127.

[79] Rafizadeh, M.; Ranjbar,; Amani, V. *Acta Crystallogr., Sect.E: Struct. Rep. Online* **2004**, *60*, m479.

[80] Rafizadeh, M.; Ranjbar,; Amani, V. *Anal. Sci.: X-Ray Struct. Anal. Online* **2005**, *21*, x113.

[81] Cai, M.; Gao, X.; Chen, J. *J. Mol. Struct.* **2015**, *1086*, 93.

[82] Viveros-Andrade, A.; Colorado-Peralta, R.; Flores-Alamo, M.; Castillo-Blum, S.; Duran-Hernandez, J.; Rivera, J. *J. Mol. Struct.* **2017**, *1145*, 10.

[83] Shankar, K.; Baruah, J. *Polyhedron* **2017**, *126*, 262.

[84] Subramani, B.; Sugumar, R. W. *J. Chem. Pharm. Res.* **2014**, *6*, 1895.

[85] Zeng, X.-Z.; Zhang, A.-Y.; He, C.; Li, Y.-W. *Chin. J. Inorg. Chem* **2013**, *29*, 1557–1562.

[86] Chen, L.; Yin, X.-H.; Tan, M.-Y.; Xia, C.-G.; Yu, K.-B. *Acta Crystallogr., Sect.E: Struct. Rep. Online* **2014**, *58*, m666.

[87] Aghabozorg, H.; Nakhjavan, B.; Ghadermazi, M.; Ramezanipour, F. *Acta Crystallogr., Sect.E: Struct. Rep. Online* **2014**, *62*, m1527.

[88] Sharif, S.; Khan, B.; Sahin, Q.; Khan, I. *Russ. Coord. Chem.* **2016**, *42*, 56.

[89] Brouca-Cabarrecq, C.; Dexpert-Ghys, J.; Fernandes, A.; Jaud, J.; Trombe, J. *Inorg. Chim. Acta* **2008**, *361*, 2909.

[90] Hou, K.-L.; Bai, F.-Y.; Xing, Y.-H.; Cao, Y.-Z.; Wei, D.-M.; Niu, S.-Y. *J. Inorg. Organomet. Polym. Mater* **2011**, *21*, 213.

[91] D'Aleo, A.; Pompidor, G.; Elena, B.; Vicat, J.; Baldeck, P.; Toupet, L.; Kahn, R.; Andraud, C.; Maury, O. *ChemPhysChem* **2007**, *8*, 2125.

[92] Cary, S. K.; Silver, M. A.; Liu, G.; Wang, J. C.; Bogart, J. A.; Stritzinger, J. T.; Arico, A. A.; Hanson, K.; Schelter, E. J.; Albrecht-Schmitt, T. E. *Inorg. Chem.* **2015**, *54*, 11399–11404.

[93] Das, B.; Baruah, J. *Cryst.Growth Des.* **2010**, *10*, 3242–3249.

[94] Shannon, R. D. Revised effective ionic radii and systematic studies of interatomic distances in halides and chaleogenides. *Acta Cryst.* **1976**, *A32*, 751.

[95] David, F. H.; Fourest, B. *New J. Chem.* **1997**, *21*, 167–176.

[96] D'Angelo, P.; Zitolo, A.; Migliorati, V.; Chillemi, G.; Duvail, M.; Vitorge, P.; Abadie, S.; Spezia, R. Revised ionic radii of lanthanoid(III) ions in aqueous solution. *Inorg. Chem.* **2011**, *50*, 4572–4579.

[97] Choppin, G. Solution chemistry of the actinides.. *Radiochim. Acta* **1983**, *32*, 43–54.

[98] McCann, K.; Laane, J. Raman and infrared spectra and theoretical calculations of dipicolinic acid, dinicotinic acid, and their dianions. *J. Mol. Struc.* **2008**, *890*, 346–358.

[99] Rota, J. B.; Knecht, S.; Fleig, T.; Ganyushin, D.; Saue, T.; Neese, F.; Bolvin, H. Zero-field splitting of the chalcogen diatomics using relativisitic correlated wavefunction methods. *J. Chem. Phys.* **2011**, 114106.

[100] Viciano-Chumillas, M.; Koprowiak, F.; Mutikainen, I.; Wernsdorfer, W.; Mallah, T.; Bolvin, H. Hysteresis in a bimetallic holmium complex: A synergy between electronic and nuclear magnetic interactions. *Phys. Rev. B* **2017**, *96*, 214427.

[101] Huang, Q.-R.; Kingham, J. R.; Kaltsoyannis, N. The strength of actinide-element bonds from the quantum theory of atoms-in-molecules. *Dalton Trans.* **2015**, *44*, 2554–2566.

[102] Cremer, D.; Kraka, E. Chemical bonds without bonding electron density- Does the difference electron-density analysis suffice for a description of the chemical bond?. *Angew. Chem. Int. Ed.* **1984**, *23*, 627–628.

[103] Gagliardi, L.; Lindh, R.; Karlström, G. Local properties of quantum chemical systems: The LoProp approach.. *J. Chem. Phys.* **2004**, *121*, 4494–4500.

[104] Carnall, W.; Goodman, G.; Williams, C.; Lam, S.; Jursich, G. Interpretation of tetravalent actinide spectra. *J. Less Common Met.* **1989**, *148*, 201–205.

[105] Jørgensen, C. K. The interelectronic repulsion and partly covalent bonding in transition-group complexes. *Discuss. Faraday Soc.* **1958**, 110–115.

[106] Bolvin, H. d-d spectrum ang high-spin/low-spin competition in d6 octahedral coordination compounds: ab initio study of potential energy curves. *J. Phys. Chem. A* **1998**, *102*, 7525.